J. Fluid Mech. (1987), *vol.* 178, *pp.* 161–175
Printed in Great Britain

Rayleigh–Taylor instability of fluid layers

By G. R. BAKER,
Department of Mathematics, University of Arizona, Tucson, AZ 85721, USA

R. L. McCRORY, C. P. VERDON
Laboratory for Laser Energetics, University of Rochester, NY 14627, USA

AND S. A. ORSZAG
Applied and Computational Mathematics, Princeton University, NJ 08540, USA

(Received 7 March 1985 and in revised form 6 October 1986)

It is shown that the Rayleigh–Taylor instability of an accelerating incompressible, inviscid fluid layer is the result of pressure gradients, not gravitational acceleration. As in the classical Rayleigh–Taylor instability of a semi-infinite layer, finite fluid layers form long thin spikes whose structure is essentially independent of the initial thickness of the layer. A pressure maximum develops above the spike that effectively uncouples the flow in the spike from the rest of the fluid. Interspersed between the spikes are rising bubbles. The bubble motion is seriously affected by the thickness of the layer. For thin layers, the bubbles accelerate upwards exponentially in time and the layer thins so rapidly that it may disrupt at finite times.

1. Introduction

Several studies (Fraley *et al.* 1974; Mason 1975) have indicated that thin-shell fusion targets have potential advantages in reducing the peak laser driving power for given performance of an inertial confinement device. Unfortunately, performance is limited by hydrodynamic instability. Two-dimensional numerical simulations (Verdon *et al.* 1982) of ablatively accelerated thin-shell fusion targets show that the essential dynamics of strongly driven flows are governed by the classical Rayleigh–Taylor instability of an ideal, incompressible, thin fluid layer.

Actually, the Rayleigh–Taylor instability appears in many natural phenomena and technical applications (Sharp 1984). In its simplest form, the onset of the instability occurs when a lighter fluid pushes a heavier fluid. The general features are for interfacial protuberances to grow and interact in complicated ways. Although several factors, such as compressibility and viscosity, may modify the behaviour, it is the density ratio that plays the most important role, but even for the simplest case of inviscid, incompressible fluids, a full treatment of the late stages of the interfacial motion is still beyond numerical studies. Consequently, the focus of most studies has been on the initial stages of the instability under ideal circumstances. For example, the classical Rayleigh–Taylor instability of a semi-infinite layer of ideal, incompressible fluid has been studied extensively (Daly 1967; Baker, Meiron & Orszag 1980; Menikoff & Zemach 1983). In particular, the two-dimensional evolution of an initial sinusoidal perturbation to the fluid surface shows the formation of long thin spikes nearly in free fall under the action of gravity, interspersed with rising bubbles that penetrate the fluid with nearly constant speed. Initially the spike growth is exponential but it soon tapers off to the quadratic growth in time characteristic of free fall. At an intermediate time, a pressure maximum forms above the spike which causes the spike to accelerate momentarily faster than gravity and which subsequently serves as a barrier between the motion of the fluid in the spike, and the rest of the fluid.

In this paper, we present results for the two-dimensional evolution of a finite layer of ideal, incompressible fluid undergoing Rayleigh–Taylor instability due to either gravity or an externally applied pressure field that accelerates the layer. The rise of the bubble is strongly affected by the thickness of the layer. The development of the pressure maximum above the spike has important consequences for the dynamics of the motion, leading in some cases to the formation of a small jet of fluid shooting out in a direction opposite to the spike. The present paper corrects some technical deficiencies present in earlier calculations of fluid layer instability and resolves some paradoxical behaviour of these layers (Verdon *et al.* 1982).

2. Formulation of problem

A horizontal layer of ideal, incompressible fluid of density ρ and uniform thickness H is initially at rest. This state is unstable in that a small initial perturbation of the layer results in large subsequent deformations. The resulting flow is assumed two-dimensional and 2π-periodic in the horizontal direction, x. In figure 1, a schematic of the flow geometry is given. The lower and upper surfaces are parametrized by $(x_1(\alpha), y_1(\alpha))$ and $(x_2(\alpha), y_2(\alpha))$ respectively where $(x(\alpha+2\pi), y(\alpha+2\pi)) = (x(\alpha)+2\pi, y(\alpha))$. An external pressure difference is applied across the layer with the pressure below and above the layer denoted by P_1 and P_2 respectively. The gravitational acceleration g is assumed to be in the y-direction. If $P_1 = P_2$, that is no applied pressure difference, the layer falls freely under gravity. Alternatively, if gravity $g = 0$ but $P_1 > P_2$ then the layer accelerates upwards with acceleration $(P_1-P_2)/\rho H$. When the pressure difference $P_1 - P_2 = \rho g H$, the layer is in static balance.

In particular, consider a perturbed layer of the form

$$(x_1(\alpha,t), y_1(\alpha,t)) = (\alpha, \tfrac{1}{2}at^2 + \epsilon_1(t)\cos(k\alpha)), \tag{2.1}$$

$$(x_2(\alpha,t), y_2(\alpha,t)) = (\alpha, H + \tfrac{1}{2}at^2 + \epsilon_2(t)\cos(k\alpha))), \tag{2.2}$$

where

$$a = (P_1 - P_2)/\rho H - g \tag{2.3}$$

is the mean acceleration of the layer. The fluid is assumed to be initially at rest with the lower surface perturbed initially by $\epsilon_0 \cos(k\alpha)$ and the top surface unperturbed. Here $\epsilon_1(0) = \epsilon_0, \epsilon_2(0) = 0$. Linearized perturbation analysis gives the result

$$\frac{2\epsilon_1}{\epsilon_0} = (1+\coth(kH))\cosh(\sigma t) + (1-\coth(kH))\cos(\sigma t), \tag{2.4}$$

$$\frac{2\epsilon_2}{\epsilon_0} = \frac{(\cosh(\sigma t) - \cos(\sigma t))}{\sinh(kH)}, \tag{2.5}$$

where the growth rate σ satisfies

$$\sigma^2 = \frac{|(P_1 - P_2)k|}{\rho H}. \tag{2.6}$$

This linear result requires some discussion. If $P_1 = P_2$, the perturbation does not grow. The layer falls uniformly under the action of gravity, g. However, if the fluid

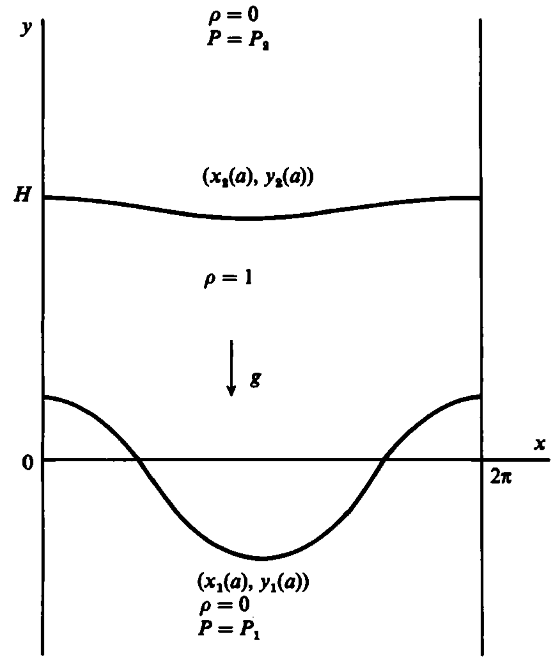

FIGURE 1. A schematic of the fluid layer.

is not initially at rest, then deformation is possible as the fluid falls (Menikoff & Zemach 1983). If $P_1 \neq P_2$, the flow is unstable for all g. We conclude that Rayleigh–Taylor instability is most properly viewed as a consequence of pressure gradients and not of gravitational acceleration. This view of Rayleigh–Taylor instability is valid for both finite and infinite fluid layers. In the next section, we present results that extend this interpretation of Rayleigh–Taylor instability to show that the nonlinear evolution of an initial, sinusoidal perturbation is independent of g except for an overall translation of the layer.

At $t = 0$, the layer is at rest so there is no initial vorticity. For ideal, incompressible flow the vorticity remains zero for all time within the layer. The fluid velocity may then be expressed as the gradient of a potential ϕ which satisfies Laplace's equation. It is convenient to introduce the complex field point $z = x + \mathrm{i}y$ and the complex potential $\Phi = \phi + \mathrm{i}\psi$ where ψ is the streamfunction. The complex velocity $q = u + \mathrm{i}v$ where u, v are the horizontal, vertical components respectively.

$$q^* = \frac{\mathrm{d}\Phi}{\mathrm{d}z}, \tag{2.7}$$

where the star superscript denotes complex conjugate.

The equations governing the evolution of the surface locations are given below. Their derivation is outlined in the Appendix.

$$\frac{\partial z_j^*}{\partial t}(\alpha) = \tilde{q}_j^*(\alpha) \equiv \frac{\Phi_{j\alpha}(\alpha) + \frac{1}{2}w_j\,\mu_{j\alpha}(\alpha)}{z_{j\alpha}(\alpha) - \mathrm{i}V(t)}, \tag{2.8}$$

where the subscript α refers to differentiation with respect to α and the subscript $j = 1, 2$ refers to values at the lower, upper surface, respectively. The weighting parameter w_j determines the tangential motion of the surface marker $z_j(\alpha)$; the choice

$w_1 = -1, w_2 = 1$ ensures that the markers move with the fluid. The complex potential at the surface generated by dipole distributions along the surfaces is given by

$$\Phi_j(\alpha) = \sum_{k=1}^{2} \int_0^{2\pi} \mu_k(\alpha')\, K_{jk}(\alpha, \alpha')\, \mathrm{d}\alpha', \tag{2.9}$$

where
$$K_{jk}(\alpha, \alpha') = \frac{1}{4\pi i} z_{k\alpha}(\alpha') \cot\{\tfrac{1}{2}(z_j(\alpha) - z_k(\alpha'))\}, \tag{2.10}$$

and it has been assumed that the layer is 2π-periodic. The principal value of the integral in (2.9) must be taken when necessary.

The rate of change of the dipole sheet strengths $(\partial u_j/\partial t)(\alpha)$ satisfy coupled Fredholm integral equations of the second kind;

$$\frac{\partial \mu_j}{\partial t}(\alpha) + A_j \sum_{k=1}^{2} \int_0^{2\pi} \frac{\partial \mu_k}{\partial t}(\alpha') \operatorname{Re}\{K_{jk}(\alpha, \alpha')\}\, \mathrm{d}\alpha' = G_j - A_j \frac{\mathrm{d}V}{\mathrm{d}t} y_j, \tag{2.11}$$

where $A_1 = -2, A_2 = 2$ and

$$G_j = -A_j \sum_{k=1}^{2} \int_0^{2\pi} \mu_k(\alpha') \operatorname{Re}\{\dot{K}_{jk}(\alpha, \alpha')\}\, \mathrm{d}\alpha' + A_j \left(\frac{\frac{1}{2}(\Phi_{j\alpha} \Phi_{j\alpha}^* + w_j \mu_{j\alpha} \operatorname{Re}(\Phi_{j\alpha}))}{z_{j\alpha} z_{j\alpha}^*} - P_j - g y_j \right) - \frac{\frac{1}{2}(\frac{1}{4}A_j - w_j)\, \mu_{j\alpha}^2}{z_{j\alpha} z_{j\alpha}^*}. \tag{2.12}$$

The kernel $\dot{K}_{jk}$ in the integral in (2.12) is given by

$$\dot{K}_{jk}(\alpha, \alpha') = \tilde{q}_{k\alpha}(\alpha') \cot\{\tfrac{1}{2}(z_j(\alpha) - z_k(\alpha'))\} - \tfrac{1}{2} z_{k\alpha}(\alpha')\, (\tilde{q}_j(\alpha)) - \tilde{q}_k(\alpha'))\, \csc^2\{\tfrac{1}{2}(z_j(\alpha) - z_k(\alpha'))\tag{2.13}$$

Finally, the translational velocity $V(t)$ is determined by

$$4 \frac{\mathrm{d}V}{\mathrm{d}t}(t) \sum_{k=1}^{2} \int_0^{2\pi} \tau_k(\alpha')\, y_k(\alpha')\, \mathrm{d}\alpha' = \sum_{k=1}^{2} \int_0^{2\pi} A_k \tau_k(\alpha')\, G_k(\alpha')\, \mathrm{d}\alpha', \tag{2.14}$$

where τ_j satisfies the adjoint, coupled Fredholm integral equations of the second kind:

$$\tau_j(\alpha) = A_j \sum_{k=1}^{2} \int_0^{2\pi} \tau_k(\alpha') \operatorname{Re}\{K_{jk}^{\dagger}(\alpha, \alpha')\}\, \mathrm{d}\alpha', \tag{2.15}$$

where
$$K_{jk}^{\dagger}(\alpha, \alpha') = \frac{1}{4\pi i} z_{j\alpha}(\alpha) \cot\{\tfrac{1}{2}(z_j(\alpha) - z_k(\alpha')). \tag{2.16}$$

Equation (2.16) corrects a typographical error in equation (4.9) of Baker (1983). The translational velocity $V(t)$ provides the necessary vertical flux so that the centroid of the fluid layer moves according to Newton's laws as the layer distorts. Indeed the motion of the centroid provides a diagnostic on the numerical calculations. Since the layer is assumed periodic, it is only the y-location $\bar{y}$ of the centroid that is meaningful:

$$4\pi H \bar{y} = \int_0^{2\pi} \{y_2^2(\alpha)\, x_{2\alpha}(\alpha) - y_1^2(\alpha)\, x_{1\alpha}(\alpha)\}\, \mathrm{d}\alpha, \tag{2.17}$$

where
$$H = \int_0^{2\pi} \{y_2(\alpha) - y_1(\alpha)\}\, \mathrm{d}\alpha, \tag{2.18}$$

is the mean thickness of the layer which remains constant in time. The vertical velocity of the centroid is given by

$$2\pi H \frac{\mathrm{d}\overline{y}}{\mathrm{d}t} = \int_0^{2\pi} y_1(\alpha)\,\mathrm{Im}\,\{\tilde{q}_1^*(\alpha)\,z_{1\alpha}(\alpha)\} - y_2(\alpha)\,\mathrm{Im}\,\{\tilde{q}_2^*(\alpha)\,z_{2\alpha}(\alpha)\}\,\mathrm{d}\alpha, \tag{2.19}$$

while its acceleration must satisfy

$$\frac{\mathrm{d}^2\overline{y}}{\mathrm{d}t^2} = -g + \frac{P_1 - P_2}{\rho H}. \tag{2.20}$$

Equations (2.17), (2.19), (2.20) are used as the diagnostics.

Equations (2.8), (2.11) and (2.14) constitute a set of evolution equations for the surfaces of the layer. They may be solved numerically as follows. Markers along the surfaces are evenly spaced in the Lagrangian variable, α. Since α is defined only by the requirement that it labels a marker that moves with the field, there is great flexibility in prescribing the initial location of the markers. We have found it convenient to use

$$z_{1j} = \overline{\alpha}_j + \mathrm{i}\epsilon_0 \cos(\overline{\alpha}_j), \tag{2.21}$$

$$z_{2j} = \overline{\alpha}_j + \mathrm{i}H, \tag{2.22}$$

where

$$\overline{\alpha}_j = \frac{j2\pi}{N} - a \sin\left(\frac{j2\pi}{N}\right) \quad (j = 0, 1, \ldots, N), \tag{2.23}$$

which describes a layer of thickness H whose lower surface has been disturbed sinusoidally. The parameter a, $0 \leqslant a < 1$, determines the initial clustering of markers in the bubble region. As t increases, the markers fall into the spike. The advantage of this labelling is that the bubble region is better represented at later times than it would be with initially uniform marker spacing. For the results reported here, $a = 0.5$. An alternative procedure (Pullin 1982) would be to make the weighting parameters w_1 and w_2 (see (2.8)) functions of the Lagrangian variable α so that points do not move significantly away from the bubble region, but those near the spike still fall into it. Some test runs using this approach showed no appreciable difference from the case where w_1 and w_2 are kept fixed, consistent with our observations that the resolution of the spike region is the dominant factor in the efficient execution of the numerical method.

The integrals are evaluated using an alternate point, trapezoidal rule after they have been regularized in a standard way (Menikoff & Zemach 1983; Baker 1983; Baker & Shelley 1986). For example, consider the integral,

$$\Phi(\alpha) = \frac{1}{4\pi \mathrm{i}} \oint_0^{2\pi} \mu(\alpha')\,z_\alpha(\alpha') \cot\{\tfrac{1}{2}(z(\alpha) - z(\alpha'))\}\,\mathrm{d}\alpha', \tag{2.24}$$

which is one of the integrals in (2.9) with the subscripts dropped. Since $\Phi(\alpha) = 0$ when $\mu(\alpha)$ is a constant, the singularity in (2.24) may be easily removed and the integrand has a finite value as $\alpha' \to \alpha$, but the limit involves the derivative of μ. However, the trapezoidal rule applied at alternate points avoids the need to evaluate the integrand at $\alpha' = \alpha$. Specifically,

$$\Phi(j\Delta e) = \frac{1}{2N\mathrm{i}} \sum_{\substack{k=1 \\ j+k=\mathrm{odd}}}^{N} (\mu(k\Delta e) - \mu(j\Delta e))\,z_\alpha(k\Delta e) \cot\{\tfrac{1}{2}(z(j\Delta e) - z(k\Delta e))\},$$

where $\Delta e = 2\pi/N$. For the non-singular integrals in (2.9), the standard trapezoidal rule is applied without any modification to the integrand. The integrals in (2.12) and

(2.15) may be treated similarly. However, difficulties in evaluating non-singular integrals accurately occur when any part of the layer is only a few times thicker than the local spacing of markers (Maskew 1977); while the interface may be well resolved, there will be too few collocation points to resolve the rapid variation in the integrand due to the nearby presence of the pole singularity. Specifically, this situation occurs when the local spacing between surface points near the field point is greater than one-sixth of the shortest distance to the other surface. Accuracy in the evaluation of these integrals may be restored by cubic spline interpolation of N new quadrature points along the interface (Baker & Shelley 1986). These new points are clustered along the interface in the vicinity of the most rapid variation in the integrand, so that the local spacing of points is at most one-sixth of the shortest distance to the other interface. Note that these quadrature points do not replace the surface-representation points but are merely introduced to evaluate the integrals accurately. Clearly, any number of quadrature points could be used that lead to accurate evaluations of the integrals, but the choice of using the same number as there are surface-representation points proves adequate for our purposes and helps keep the computational cost moderate.

The value of $\partial\mu_j/\partial t$ is computed by collocation and may be found iteratively from the discrete form (2.11) since the Fredholm integral equations have a globally convergent Neumann series. A solution is considered converged whenever the absolute value of the difference between two iterates of $\partial\mu/\partial t$ is less than 10^{-7} at each collocation point. Improved first guesses for the solution are obtained from a fourth-order extrapolation of data from previous time levels. Unfortunately, the eigenvalues of the iteration procedure approach 1 as the layer thins, requiring many more iterations for convergence and at the same time the more costly procedure of interpolating new quadrature points must be used.

All derivatives are evaluated from cubic-spline approximations with fourth-order accuracy. Second-order derivatives may be calculated also with fourth-order accuracy by fitting a cubic spline to the first-order derivatives (Shelley & Baker 1986). Time integration is performed using the standard fourth-order Adams–Moulton predictor–corrector; starting values are obtained with the fourth-order Runge–Kutta method. Consequently, the method has an overall accuracy which is fourth-order in both time and space. Several tests were performed to check the computer code. In particular, a third-order perturbation expansion was used as an exact solution for small time and the numerical results showed clearly the fourth-order accuracy of the method.

The numerical stability of the method is much more difficult to assess. Our calculations show no evidence of numerical instability, neither in the results reported here nor in previous work (Baker *et al.* 1980, 1982). Others who have also used boundary integral techniques to study Rayleigh–Taylor instability, report instabilities in the bubble region. Linear analysis suggests that the flow in the bubble region is unstable, but a more thorough analysis (Dagan 1975) shows that the growth rates are reduced by the stretching of the interface. Thus, the stability of the bubble remains an open question, not easily resolved by numerical studies.

3. Results

Several special cases have been used to verify the reliability of the computer code. With $p_1 = p_2 = 0$ but $g = 1$, the fluid layer falls without deformation and the centroid moves according to $\bar{y} = \bar{y}_0 - 0.5t^2$ where $\bar{y}_0$ is the initial position of the centroid. With

$N = 33$ markers and a time step $\Delta t = 0.005$, the numerical code was used to follow a layer of thickness $H = 0.25$ and initial perturbation amplitude $\epsilon_0 = 0.1$ until $t = 1$ with only roundoff errors being observed. This result is expected since the variation in time is quadratic so it should be treated accurately to within roundoff error by the fourth-order Adams–Moulton predictor–corrector scheme.

Next a comparison was made between a layer accelerated by a pressure difference $P_1 = H = 0.25$, $P_2 = 0$ without gravity ($g = 0$) and with gravity ($g = 1$). When $g = 0$, the centroid accelerates vertically at rate 1, while, if $g = 1$, the centroid remains fixed. Theoretically the location of the surfaces relative to the centroid is the same in both cases. With $N = 33$ and $\Delta t = 0.005$, the agreement in numerical results for the two cases was good to 10^{-5} in the time interval $(0, 1.5)$.

For our main results, we used $P_1 = H, P_2 = 0$ and $g = 1$ so that the centroid remained stationary. Clearly the results can depend on only two non-dimensional parameters kH and ϵ_0/H where k is the wavenumber and ϵ_0 is the amplitude of the initial perturbation on the lower surface. In all cases reported here, the initial perturbation had only one Fourier mode and so we chose $k = 1$. Unless otherwise stated, $N = 64$ points were used to represent each surface over a full wavelength and the timestep was 0.005 for the results reported here. Of course, computer runs with less points and larger timesteps were also done to check accuracy. Another check on accuracy is provided by the computation of $\mathrm{d}\bar{y}/\mathrm{d}t$ ($= 0$ for the cases considered here) by (2.19). In general, the error in $\mathrm{d}\bar{y}/\mathrm{d}t$ is larger than the error in the location of the interface. The largest errors occur at the end of the calculations; there is a dramatic rise in the error in $\mathrm{d}\bar{y}/\mathrm{d}t$ from 10^{-5} and better to about 10^{-1} when the code stopped. Thus we are confident in the accuracy of the results.

First the dependency on H is studied, so $\epsilon_0 = 0.5$ was kept fixed and several calculations with various H were done. In figure 2, the location of the surfaces of the layer are shown at three times for $H = 10$. Only a half wavelength is shown, and the surface points are marked by a small x. In addition to the layer boundaries, contours of constant pressure are shown as dashed curves. These contours show that the main pressure gradient remains largely unaffected above the bubble, but that a pressure maximum develops above the spike. Figure 3 shows the pressure along the centreline of the spike and the development of the pressure maximum is clearly observable. While the behaviour of the lower surface appears identical to that of a semi-infinite fluid undergoing the classical Rayleigh–Taylor instability (Daly 1967), there are some differences. In particular, the rise of the bubble is affected by the finite thickness of the layer. In figure 4, the velocity V_b of the bubble as defined by the vertical velocity at the bubble centre on the lower surface is shown as a function of time for various layer thickness. The bubble always rises faster than bubbles generated by the classical Rayleigh–Taylor instability of a semi-infinite fluid layer, although the comparison is complicated by the question of the frame of reference. For finite layers, measurements are made relative to the centroid of a periodic strip, but in the semi-infinite fluid the centroid loses its meaning and measurements are done in a frame where there is no motion at ∞. That is, in the semi-infinite case, the frame is defined so there is no mean flux across the surface. For the finite-layer calculations, there is a mean flux across the bounding surfaces. A suitable vertical velocity may be subtracted from the bubble velocity of the layer so that there is no mean flux across the top and bottom surfaces (but the centroid now moves); the results in this modified reference frame are drawn as dashed lines in figure 3. There is now closer agreement with the classical Rayleigh–Taylor result for the large-time Froude number $V_b/(g\lambda)^{\frac{1}{2}} \approx 0.225$ ($\lambda = 2\pi$ in our calculations) although the difference is still $O(1/H)$. At very large times, the

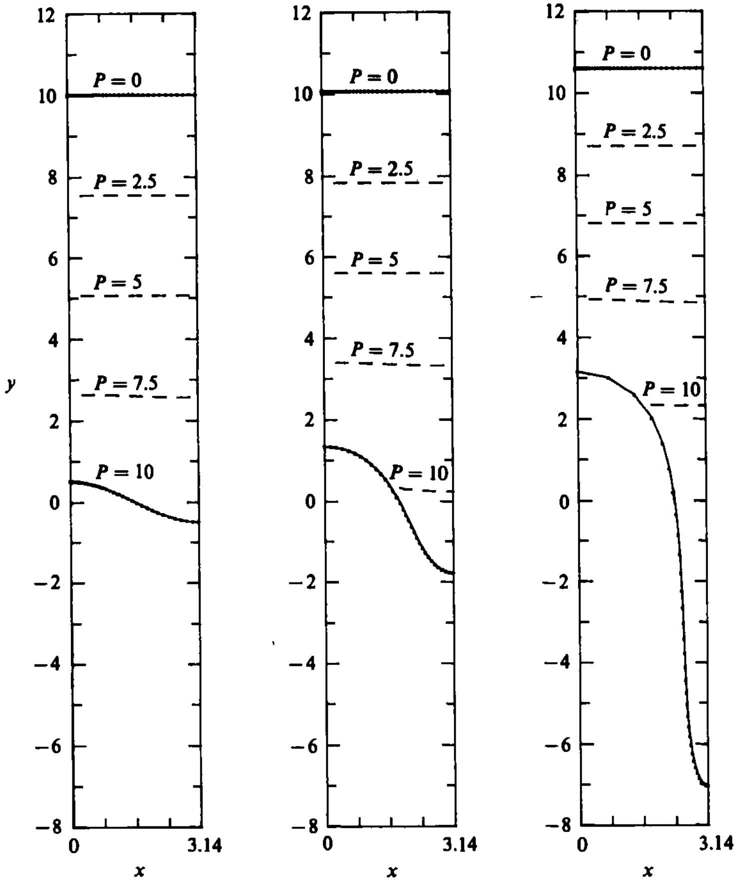

FIGURE 2. A periodic window showing the surfaces of the fluid layer (solid curves) and contours of constant pressure (dashed lines) for various times: the layer has thickness $H = 10$. (*a*) $t = 0$; (*b*) $t = 2$; (*c*) $t = 4$.

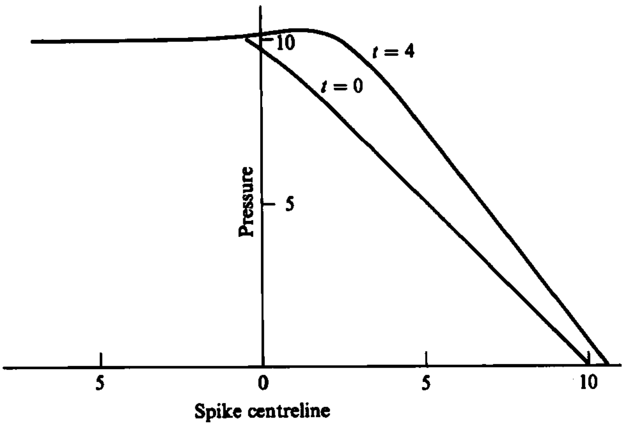

FIGURE 3. Pressure profiles at $t = 0$ and $t = 4$ along the centreline of the spike ($x = \pi$) for the same run as in figure 2.

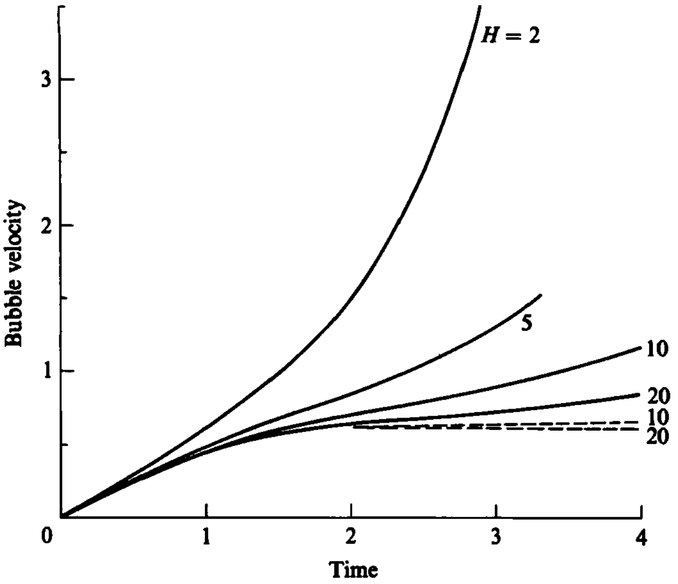

FIGURE 4. Bubble velocity determined at $x = 0$ on the lower surface as a function of time for various H (solid curves); the same in a frame with no vertical flux (dashed lines).

bottom surface of a finite layer gets close to its top surface and the bubble begins to accelerate upwards; for thick layers, this occurs at a time $O(H)$. For thicknesses less than about half a wavelength, the bubble motion is completely different from that of the classical Rayleigh–Taylor instability; the bubble continually accelerates upwards at an exponentially increasing rate.

In figure 5, the location of the layer boundaries are shown at various times for $H = 2.0$. The bubble becomes a thin layer of fluid draining into a well-formed spike. Notice the formation of an anti-spike on the top surface. The anti-spike is a jet of fluid that falls back on itself due to the presence of gravity. Alternatively one may consider the anti-spike as a hydraulic jump that results from fluid draining out of the bubble and falling rapidly into the trough formed by the spike. The fine-scale structure of the anti-spike is too difficult to resolve without exorbitant computing costs, so our results are terminated at the intermediate stages of the anti-spike formation. The pressure contours show the formation of a very large pressure maximum above the spike, consistent with the behaviour of the fluid. The pressure profile along the centreline of the spike is shown in figure 6.

Assuming that the motion of a layer of incompressible, inviscid fluid is well posed for all time, it is likely that the pattern of behaviour plotted in figure 5 occurs for all layer thickness H. For large H, we expect that the time at which the top surface begins to deform into an anti-spike is substantial. Therefore, it is most efficient to infer results for general H from those for thin layers in which efficient computations can be done.

In figure 7, the bubble rise velocity in time is shown for various H but with $\epsilon_0/H = 0.2$ kept fixed. The trend is similar in all cases showing that the bubble depends on ϵ_0/H and only weakly on kH. However the acceleration of the tip of the spike depends on $\epsilon_0 k$ and only weakly on kH. The behaviour of the spike is similar to its behaviour in the classical Rayleigh–Taylor instability (see figure 8).

It seems that as the bubble accelerates upwards, the layer thins rapidly and may eventually disrupt. In figure 9, we plot the bubble thickness as a function of time.

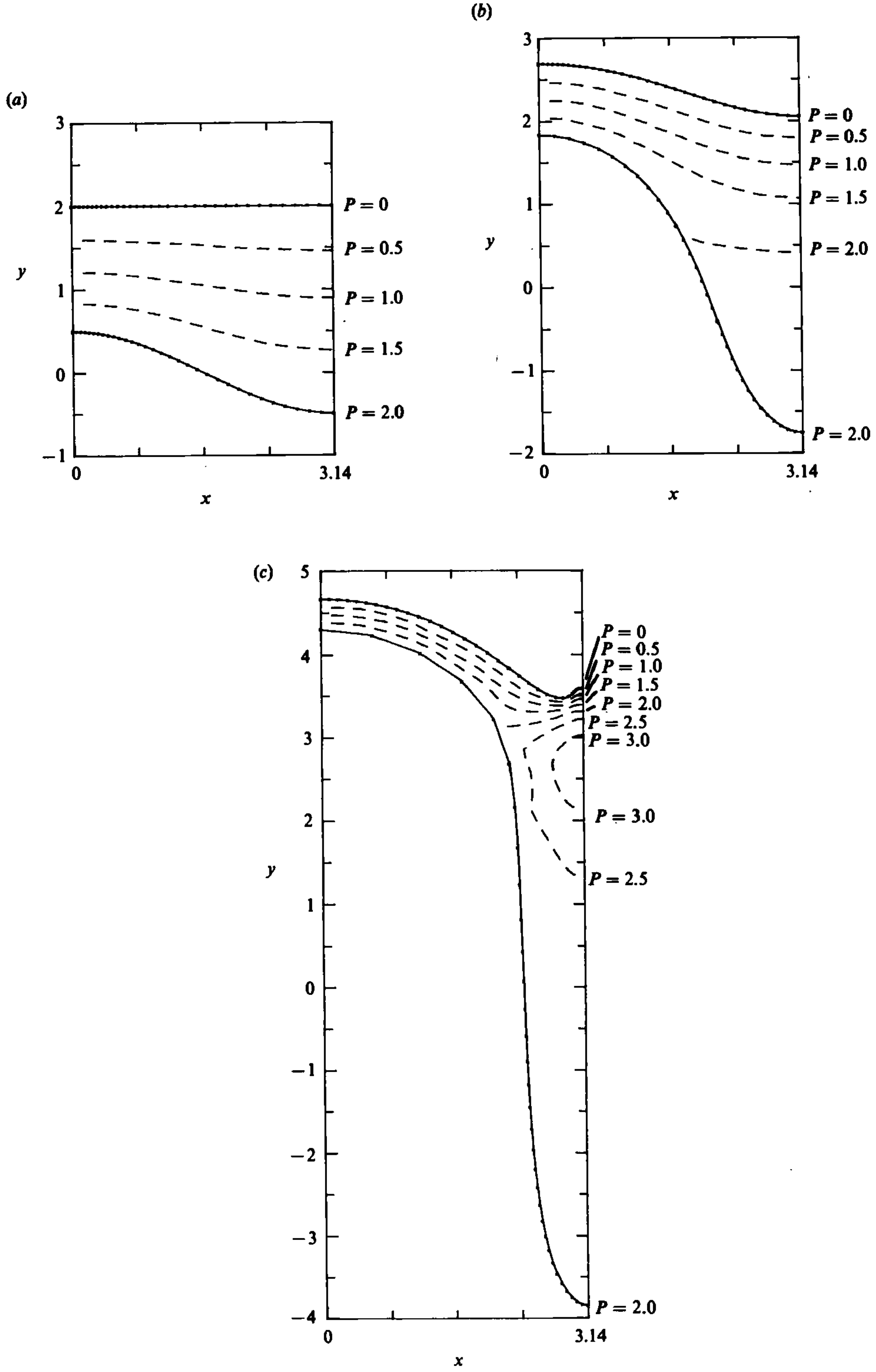

FIGURE 5. A periodic window showing the surfaces of the fluid layer (solid curves) and contours of constant pressure (dashed lines) for various times; the layer has thickness $H = 2.0$. (*a*) $t = 0$; (*b*) $t = 2$; (*c*) $t = 3$.

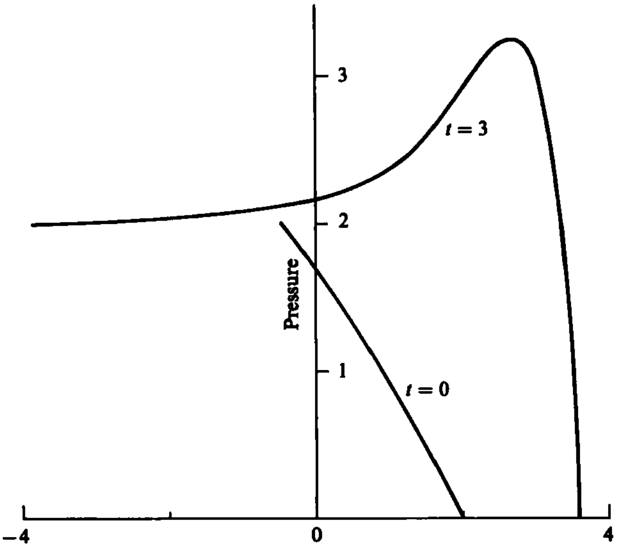

FIGURE 6. Pressure profiles at $t = 0$ and $t = 3$ along the centreline of the spike ($x = \pi$) for the same run as in figure 5.

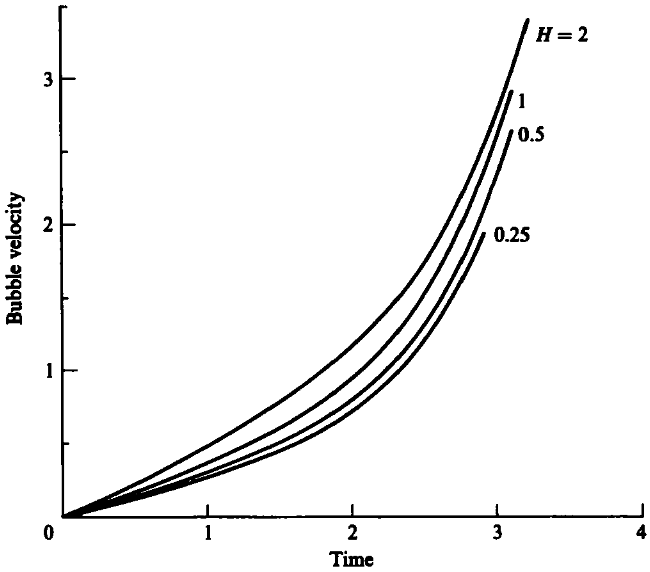

FIGURE 7. Bubble velocity determined at $x = 0$ on lower surface as a function of time for various H.

For $H = 1.0$ and 2.0 the thinning appears exponential at large times. Since the bubble is rising nearly exponentially for these very thin layers, this implies that the amount of fluid in the bubble region is remaining almost constant. There is an apparent uncoupling of the motion of the spike and bubble at late times through the formation of a pressure maximum just below the top surface above the spike. This pressure maximum prevents fluid from draining out of the bubble, allows the fluid in the spike to fall with gravity, and causes the anti-spike to form.

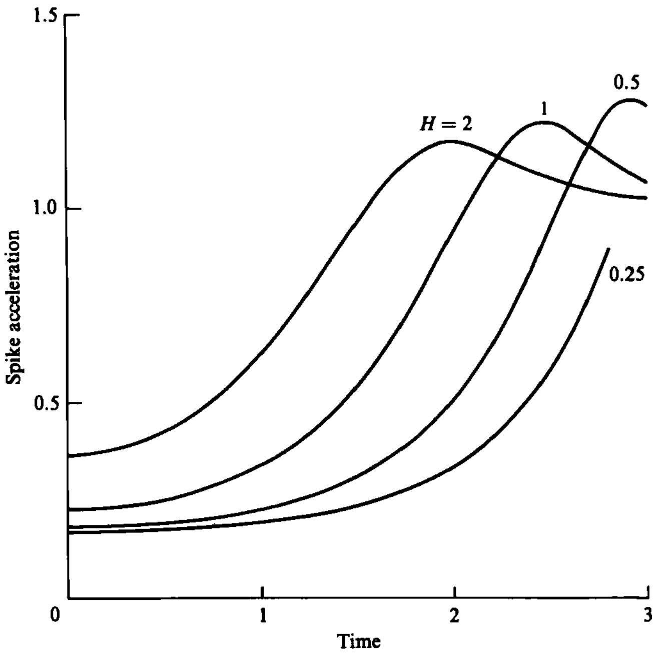

FIGURE 8. Spike acceleration determined at $x = \pi$ on lower surface as a function of time for various H.

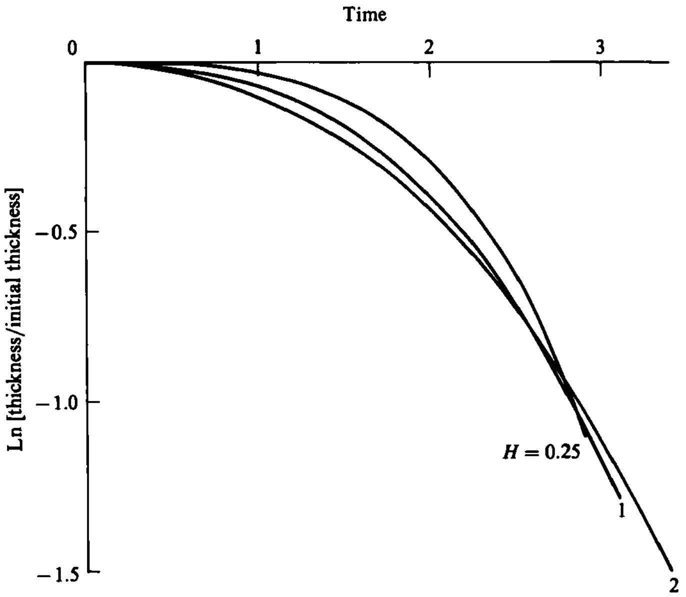

FIGURE 9. Layer thickness determined at $x = 0$ as a function of time for various H.

Since the anti-spike begins to form at about $t = 3$ for $H = 0.5$, 1.0 and 2.0 (as determined by the presence of a negative curvature on the top surface above the spike), it seems possible that enough fluid may drain out of the bubble of a layer whose thickness is much less than 1 and that the bubble disrupts before the pressure maximum forms. Indeed the rate of decrease of the bubble thickness for $H = 0.25$

($N = 128$ points were used) is apparently faster than exponential when the calculation had to be terminated due to lack of resolution of the integrands in the region of the bubble. However our calculations may not be sufficiently accurate at late times so that the possibility of the bubble disrupting in finite time must remain open. Of course, even if the decay is always exponential, the bubble becomes thin enough after a reasonable time that for practical purposes the bubble may be considered disrupted.

In conclusion, it is clear that the limitation on the amount of fluid in a layer seriously affects the Rayleigh–Taylor instability. While the spike always accelerates nearly in free fall at large times, the bubble no longer rises with constant velocity but also accelerates, apparently without bound. The thickness of the bubble region appears to decay exponentially in time for layers that are initially moderately thick. However, for initially very thin layers, it seems that the layer may disrupt after finite time even for ideal fluid flow.

We wish to acknowledge some very useful discussions with Drs R. Menikoff and T. Hussey. This work was supported by the Lawrence Livermore National Laboratory, which is supported by the Department of Energy.

Appendix

There are several, alternate boundary-integral formulations for free-surface flow, but those based on dipole distributions along the surface offer many advantages over other representations (Baker *et al.* 1982). In particular, the integrals are easier to evaluate numerically and the integral equations may be solved efficiently by iterative techniques. However, for multi-connected domains, a source external to the domain must augment the dipole representation. In the two-dimensional, periodic geometry that we have assumed for our calculations, the source is placed at infinity and the additional complex potential is $-\mathrm{i}Vz$, where V is a vertical velocity related to the mean flux across the surfaces. The value of V must be determined by the dynamical requirements of the flow.

The complex potential generated by dipole distributions μ_k along the surfaces is given by

$$\left.\begin{aligned}\Phi(z) &= \frac{1}{2\pi\mathrm{i}}\sum_{k=1}^{2}\int_{-\infty}^{\infty}\frac{\mu_k(\alpha)\,z_{k\alpha}(\alpha)}{z-z_k(\alpha)},\\ &= \frac{1}{4\pi\mathrm{i}}\sum_{k=1}^{2}\int_{0}^{2\pi}\mu_k(\alpha)\,z_{k\alpha}(\alpha)\cot\{\tfrac{1}{2}(z-z(\alpha))\}\,\mathrm{d}\alpha.\end{aligned}\right\} \tag{A 1}$$

The periodic contributions along the surface have been summed up into closed form (Menikoff & Zemach 1983) and the notational conventions introduced in §2 have been adopted here. The potential at the surface, $\Phi_j(\alpha)$, is given by the principal value of the integrals, which is (2.9). Similarly, the tangential velocity at the surfaces jumps in value, but the normal velocity is continuous as required kinematically. Consequently, there is some arbitrariness in the definition of the motion of surface markers. A common choice is the average velocity which is given by $\Phi_{j\alpha}/z_{j\alpha}$, but there are important advantages in using a weighted average $(\Phi_{j\alpha}+\frac{1}{2}w_j\mu_{j\alpha})/z_{j\alpha}$, where w_j is the weighting parameter. The particular choices $w_j = -1, +1$ mean that the markers move with the upper, lower fluid respectively. Note that even if the density is zero on one side of the interface, the potential (A 1) still provides a kinematically correct flow field in that region. For the calculations reported here, w_j is always chosen so that the markers move with the fluid in the layer. The motion of the surfaces is therefore described by (2.8) which includes the source contribution. The use of a partial time derivative is to emphasize that the motion keeps the marker label α fixed.

Bernoulli's equation evaluated at the surface gives

$$\frac{\partial \phi_{fj}}{\partial t} - \tilde{u}_j u_{fj} - \tilde{v}_j v_{fj} + \tfrac{1}{2}(u_{fj}^2 + v_{fj}^2) + P_j + g y_j = 0, \tag{A 2}$$

where ϕ_{fj} is the velocity potential of the flow in the layer at the jth surface and u_{fj}, v_{fj} are the corresponding fluid velocities. The partial time derivative means that the change in ϕ_f is calculated along the trajectory of the surface marker labelled α. The potential ϕ_{fj} may be expressed in terms of the dipole distribution as

$$\Phi_{fj} = \mathrm{Re}\left(\Phi_j(\alpha) + \frac{\mu_j(\alpha)}{A_j}\right) - \mathrm{i} V z_j(\alpha). \tag{A 3}$$

Similarly, the complex fluid velocity is

$$(u_{fj} + \mathrm{i} v_{fj})^* = \frac{(\Phi_{j\alpha}(\alpha) + \mu_{j\alpha}(\alpha)/A_j)}{z_{j\alpha}} - \mathrm{i} V. \tag{A 4}$$

After substituting (A 3) and (A 4) into (A 2) and performing some simple algebra, one obtains

$$\frac{\partial \mu_j}{\partial t} + A_j \,\mathrm{Re}\left\{\frac{\partial \Phi_j(\alpha)}{\partial t}\right\} + A_j \frac{\mathrm{d}V}{\mathrm{d}t} y_j - A_j\{\tfrac{1}{2}(\Phi_{j\alpha}\Phi_{j\alpha}^* + w_j \mu_{j\alpha}\,\mathrm{Re}\,(\Phi_{j\alpha}))/z_{j\alpha} z_{j\alpha}^*$$
$$- P_j - g y_j\} + \frac{\frac{1}{2}(\frac{1}{4}A_j - w_j)\,\mu_{j\alpha}^2}{z_{j\alpha} z_{j\alpha}^*} = 0. \tag{A 5}$$

Finally, the time rate of change of the average potential may be expressed as

$$\frac{\partial \Phi_j(\alpha)}{\partial t} = \sum_{k=1}^{2} \int_0^{2\pi} \frac{\partial \mu_k(\alpha')}{\partial t} \,\mathrm{Re}\,\{K_{jk}(\alpha, \alpha')\}\,\mathrm{d}\alpha' + \sum_{k=1}^{2} \int_0^{2\pi} \mu_k(\alpha')\,\mathrm{Re}\,\{\dot{K}_{jk}(\alpha, \alpha')\}\,\mathrm{d}\alpha', \tag{A 6}$$

and when (A 6) is substituted in (A 5), (2.11) follows after some rearrangement of the terms.

Equation (2.11) has a non-trivial, homogeneous solution and so according to the Fredholm alternate, no solution to the inhomogeneous equation is possible unless (2.14) is satisfied. Consequently, for given P_j and fluid velocity, which means μ_j is known, $\mathrm{d}V/\mathrm{d}t$ is needed in Bernoulli's equation to counteract the effect of the nonlinear term which contributes a mean pressure different at each surface and which effects the balance between P_j, the hydrostatic pressure gy, and the mean acceleration of the layer.

With (2.14) satisfied, the solution to (2.11) is determined up to a constant contribution to $\partial\mu_j/\partial t$. This latter term gives a constant contribution to $\partial\phi/\partial t$ that is dynamically irrelevant and therefore chosen arbitrarily. The details of this and the numerical procedure used to solve (2.11) are available elsewhere (Baker 1983).

REFERENCES

Baker, G. R. 1983 Generalized vortex methods for free-surface flows. In *Waves on Fluid Interfaces* (ed. R. E. Meyer), pp. 53–81. MRC, University of Wisconsin, Madison.

Baker, G. R., Meiron, D. I. & Orszag, S. A. 1980 Vortex simulations of the Rayleigh–Taylor instability. *Phys. Fluids* **23**, 1485–1490.

BAKER, G. R., MEIRON, D. I. & ORSZAG, S. A. 1982 Generalized vortex methods for free-surface flow problems. *J. Fluid Mech.* **123**, 477–501.

BAKER, G. R. & SHELLEY, M. 1986 Boundary integral methods for multi-connected domains. *J. Comp. Phys.* **64**, 112–132.

DAGAN, G. 1975 Taylor instability of a non-uniform free-surface flow. *J. Fluid Mech.* **67**, 113–123.

DALY, B. J. 1967 Numerical study of two fluid Rayleigh–Taylor instability. *Phys. Fluids* **10**, 297–307.

FRALEY, G., GULA, W., HENDERSON, D., MCCRORY, R., MALONE, R., MASON, R. & MORSE, R. 1974 Implosion, stability and burn at multi-shell fusion pellets. In *Plasma Physics and Controlled Nuclear Fusion Research*, vol. 2, pp. 543–549. Tokyo, Japan. (International Atomic Energy Agency, Vienna, Austria).

MASKEW, B. 1977 Subvortex technique for the close approach to a discretized vortex sheet. *J. Aircraft* **14**, 188–196.

MASON, R. J. 1975 The calculated performance of structured laser fusion pellets. *Nuclear Fusion* **15**, 1031–1044.

MENIKOFF, R. & ZEMACH, C. 1983 Rayleigh–Taylor instability and the use of conformal maps for ideal fluid flow. *J. Comp. Phys.* **51**, 28–64.

PULLIN, D. I. 1982 Numerical studies of surface-tension effects in nonlinear Kelvin–Helmholtz and Rayleigh–Taylor instabilities. *J. Fluid Mech.* **119**, 507–532.

SHARP, D. H. 1984 An overview of Rayleigh–Taylor instability. *Physica* **12**, 31–18.

SHELLEY, M. J. & BAKER, G. R. 1987 Order preserving approximations to successive derivatives of periodic functions by iterated splines. *SIAM J. Num. Anal.* (In press).

VERDON, C. P., MCCRORY, R. L., MORSE, R. L., BAKER, G. R., MEIRON, D. I. & ORSZAG, S. A. 1982 Nonlinear effects of multi-frequency hydrodynamic instabilities on ablatively accelerating thin shells. *Phys. Fluids* **25**, 1653–1673.